J. Astrophys. Astr. (2005) **26,** 1–70

GMRT HI Observations of the Eridanus Group of Galaxies

A. Omar*[1] & K. S. Dwarakanath[2]
Raman Research Institute, Sadashivanagar, Bangalore 560 080, India.
[1]*e-mail: aomar@upso.ernet.in*
[2]*e-mail: dwaraka@rri.res.in*

Received 2004 August 23; accepted 2005 March 22

Abstract. The GMRT HI 21cm-line observations of galaxies in the Eridanus group are presented. The Eridanus group, at a distance of $\sim$23 Mpc, is a loose group of $\sim$200 galaxies. The group extends to more than 10 Mpc in projection. The velocity dispersion of the galaxies in the group is $\sim$240 km s^{-1}. The galaxies are clustered into different sub-groups. The overall population mix of the group is 30% (E + S0) and 70% (Sp + Irr). The observations of 57 Eridanus galaxies were carried out with the GMRT for $\sim$ 200 h. HI emission was detected from 31 galaxies. The channel rms of $\sim$ 1 mJy beam^{-1} was achieved for most of the image-cubes made with 4 h of data. The corresponding HI column density sensitivity (3σ) is $\sim 1 \times 10^{20}$ cm^{-2} for a velocity-width of $\sim$ 13.4 km s^{-1}. The 3σ detection limit of HI mass is $\sim 1.2 \times 10^7$ M$_\odot$ for a line-width of 50 km s^{-1}. Total HI images, HI velocity fields, global HI line profiles, HI mass surface densities, HI disk parameters and HI rotation curves are presented. The velocity fields are analysed separately for the approaching and the receding sides of the galaxies. These data will be used to study the HI and the radio continuum properties, the Tully–Fisher relations, the dark matter halos, and the kinematical and HI lopsidedness in galaxies.

Key words. Galaxies: groups, clusters—individual: Eridanus—radio lines: HI 21cm-line.

1. Motivation

Several redshift surveys carried out over the past several decades indicate that galaxies are distributed inhomogeneously in the local Universe. The regions of highest galaxy densities are superclusters and clusters. However, the majority of galaxies in the local Universe are found in less dense regions called groups. According to theories of hierarchical structure formation, clusters are built via mergers of groups. Clusters differ from groups in several aspects. A remarkable difference is observed in the morphological mix and HI content of the galaxies. Clusters have an enhanced population of both the early type (S0 and E) galaxies and the HI depleted spirals (Curtis 1918; Hubble &

*Present address: ARIES, Manora peak, Nainital 263 129, Uttaranchal, India.

Humason 1931; Davies & Lewis 1973; Giovanelli & Haynes 1985; Warmels 1988; Cayatte *et al.* 1990; Bravo-Alfaro *et al.* 2000) while groups are populated mainly by HI rich spirals. Dressler (1980) noticed a tight correlation between the galaxy morphology and the local projected galaxy density. This correlation, known as the density-morphology relation, is observed to be valid over more than five orders of magnitude in the projected galaxy density (Postman & Geller 1984). The origin of the enhanced population of E + S0s in high galaxy density regions has been the subject of much debate. There are two hypotheses for the formation of S0s, one is "Nature" where it is believed that early types were formed as such, and the other is "Nurture" according to which S0s are transformed spirals. Some of the recent observations indicate that the clusters at intermediate redshifts ($z \sim 0.1 - 0.3$) tend to have a higher fraction of S0s at the expense of spirals (e.g., Poggianti *et al.* 1999; Dressler *et al.* 1997; Fasano *et al.* 2000). These observations support the "Nurture" scenario.

Several gas-removal mechanisms, *viz.*, ram-pressure stripping (Gunn & Gott 1972), thermal conduction (Cowie & Songaila 1977), viscous stripping (Nulsen 1982), harassment (Moore *et al.* 1998), starvation, etc. have been proposed to explain the HI deficiency in cluster spirals. Some of these processes are also believed to be driving the transformation of spirals to S0s. Each of these processes has been predicted to remove HI mass of the order of the typical HI mass of a galaxy. These processes, however, are quite sensitive to several parameters like the density of the intra-cluster medium (ICM), the radial velocity vector of the galaxy, the magnetic field in the ICM, the gas-reservoir in the galaxy halo, etc. Some of these parameters have poor estimations which make the efficacy of these processes doubtful. It has been argued that no single gas-removal mechanism can explain the global HI deficiency in cluster spirals (e.g., Magri *et al.* 1988). The exact physical mechanism(s) responsible for HI depletion in cluster spirals, therefore, remains uncertain. These difficulties have led one to speculate that cluster galaxies were perhaps HI deficient even before they fell into the cluster. Such a scenario can be explored by studying groups of galaxies.

Several groups have been previously imaged in HI, e.g., the Hickson Compact Groups (HCGs; Verdes-Montenegro *et al.* 2001) and the Ursa-Major group (Verheijen & Sancisi 2001). The galaxy densities in HCGs are comparable to that in galaxy clusters, although HCGs have far less number of galaxies compared to that in clusters. The galaxies in some of the HCGs were found to be significantly HI depleted. HCGs also tend to have a significant population of early type galaxies. The Ursa-Major group, which has only a few S0s and no ellipticals, showed no significant HI deficiency. The environment in the Ursa-Major group is similar to that in field. Here, we present an HI survey of the Eridanus group of galaxies with the recently completed Giant Meterwave Radio Telescope (GMRT). The Eridanus group is believed to be at an evolutionary stage intermediate to that of field and a cluster. The Eridanus group has a significant population of early type galaxies. The sub-grouping of galaxies in the group is quite prominent. The Eridanus group also has weak diffuse X-ray emission centered around some of the brightest galaxies in the sub-groups. On a broader perspective, the properties of the Eridanus group are between that of a loose group like the Ursa-Major and a cluster like Fornax or Virgo. The main aim of this survey is to identify the galaxy evolution processes active in an environment intermediate between that of a cluster and field.

The GMRT observations provided both the HI and the radio continuum ($\nu \sim 1.4$ GHz) data. The kinematical information of galaxies has also been obtained using the H I data. This survey has capabilities to carry out several other studies. Some of the studies proposed to be carried out are the following:

- H I content of galaxies in the Eridanus group.
- H I morphologies of galaxies in the group.
- Tully–Fisher relations.
- Radio–Far-infrared correlation.
- Rotation curves and dark matter halos.
- Kinematical and H I lopsidedness.

In the present paper, the GMRT observations and the data analyses are described. We also investigate correlations between H I and optical properties in this paper. The paper is arranged in the following order. The next section describes the properties of the Eridanus group. Section 3 contains details of the GMRT observations. The analyses of the H I images are described in section 4. Some of the H I properties of the Eridanus galaxies are discussed in section 5. The results are presented in the tables in Appendix A. The H I atlas consists of the H I images, the H I velocity fields, the global H I profiles, the H I surface densities, the H I rotation curves, and the kinematical parameters of the H I disks. The H I atlases are given in Appendix B.

2. The Eridanus group

2.1 *Introduction*

The concentration of galaxies in the Eridanus region is known for many decades (Baker 1933, 1936). The complex morphology of this region was pointed out by de Vaucouleurs (1975). The Eridanus group was identified as a moderate size cluster in a large scale filamentary structure near $cz \sim 1500$ km s^{-1} in the Southern Sky Redshift Survey (SSRS; da Costa *et al.* 1988). This filamentary structure, which is the most prominent in the southern sky, extends for more than 20 Mpc in projection. The Fornax cluster and the Dorado group of galaxies are also part of this filamentary structure. The dynamical parameters of a few galaxies in the Eridanus group were first published by Rood *et al.* (1970). With the increased number of identifications in this region by Sandage & Tammann (1975) and Welch *et al.* (1975), the latter authors speculated a dynamical connection between the Fornax cluster and the Eridanus group. Using the data from the Southern Galactic Cap sample (SGC; Pellegrini *et al.* 1990), Willmer *et al.* (1989) grouped the galaxies in the Eridanus region into different sub-groups and studied their dynamics. They concluded that each sub-group is a bound structure and possibly the entire group is also gravitationally bound with a dynamical mass greater than 10^{13} M$_\odot$. They further pointed out that the Fornax and the Eridanus together constitute a bound system. The Eridanus group is a dynamically young system with a velocity dispersion of $\sim$ 240 km s^{-1}, which is lower compared to that ($\sim$ 1000 km s^{-1}) seen in clusters like the Coma. The distance to the group is estimated as 23 ± 2 Mpc based on the surface brightness fluctuation measurements (Tonry *et al.* 1997; Jensen *et al.* 1998; Tonry *et al.* 2001). All identified members in the group are in the Heliocentric velocity range of $\sim$ 1000–2200 km s^{-1}, except NGC 1400 (S0), which has a velocity of $\sim$558 km s^{-1}. However, NGC 1400 is predicted to be at a similar distance as that of the other members of the group based on the surface brightness fluctuation measurements.

2.2 *Group structure, membership, and morphological mix*

The velocity-cone diagrams are plotted in Fig. 1. The plots are in the supergalactic coordinates. The velocities obtained from the NASA Extra-galactic Database (NED) are Heliocentric, and follow the optical definition. The clustering of galaxies near $l = 283^\circ$ and $b = -43^\circ$ is the Eridanus group. Most of the galaxies are concentrated in the velocity range $cz = 1000$–2200 km s^{-1}. The group appears to be loose and irregular. The clustering of galaxies near the apex ($cz = 0$) is the local group. In Fig. 2, the positions of galaxies within the velocity range 500–2500 km s^{-1} are plotted. There are 181 galaxies in this plot, 60 early types (E + S0) and 121 late types (Sp + Irr). The approximate boundaries of three main sub-groups identified by Willmer *et al.* (1989) are marked in this figure. The sub-clustering of galaxies can be seen in this figure.

It can be seen that most of the early type galaxies are in the region inside the circle marked in Fig. 2. The sub-clustering is also prominent in the inner region. In the outer regions, population is dominated by spirals. The morphological mix is appreciably different in each sub-group. The three sub-groups namely NGC 1407, NGC 1332, and NGC 1395 have their brightest members as an elliptical or an S0. The NGC 1407 sub-group is the richest in the early types, most of them being S0s. The population of (E + S0) and (Sp + Irr) in the NGC 1407 sub-group is 70% and 30% respectively, while that in most of the other sub-groups is ~40% and 60% respectively. The overall population mix of the Eridanus group is ~30% (E + S0) and 70% (Sp + Irr). The velocity-histograms of the early types and the late types are plotted in Fig. 3. There is no appreciable difference in the velocity range over which the early types and the late types are distributed. However, it can be seen from the upper panel of Fig. 3 that the distribution of early-type galaxies is approximately a Gaussian whereas the late-type galaxies are rather uniformly distributed. Upon inspection of the locations of late-type galaxies at lower (1000–1300 km s^{-1}) and higher (1800–2100 km s^{-1}) velocity ends from the mean, it appears that the galaxies having higher velocities are more uniformly distributed in the sky compared to those at lower velocities. The lower velocity galaxies are largely confined within the circle drawn in Fig. 2. Further, it is interesting to note that the population mix of the NGC 1407 sub-group is similar to that seen in evolved clusters like the Coma, whereas the velocity dispersion (~250 km s^{-1}) of the NGC 1407 sub-group is much smaller than that of Coma (~ 1000 km s^{-1}). Some other groups like Leo I, NGC 3607, and NGC 5846, which have lower velocity dispersions compared to that in clusters are also populated mainly by early type galaxies.

2.3 *X-ray properties*

The optically bright early type galaxies NGC 1400, NGC 1407, NGC 1395, and NGC 1332 are known X-ray sources in this group. Trinchieri *et al.* (2000) reported the presence of diffuse X-ray emission around NGC 1407. The processed and calibrated X-ray images (0.1 keV–2.0 keV) centered at NGC 1407, NGC 1395, and NGC 1332 were obtained from the ROSAT PSPC (Roentgen Satellite Position Sensitive Proportional Counter) archival data. Each field was observed for ~ 6 h using the ROSAT PSPC instruments. The soft X-ray images shown in Fig. 4 were convolved with a circular Gaussian beam of FWHM 90″ to enhance the diffuse emission. Apart from the

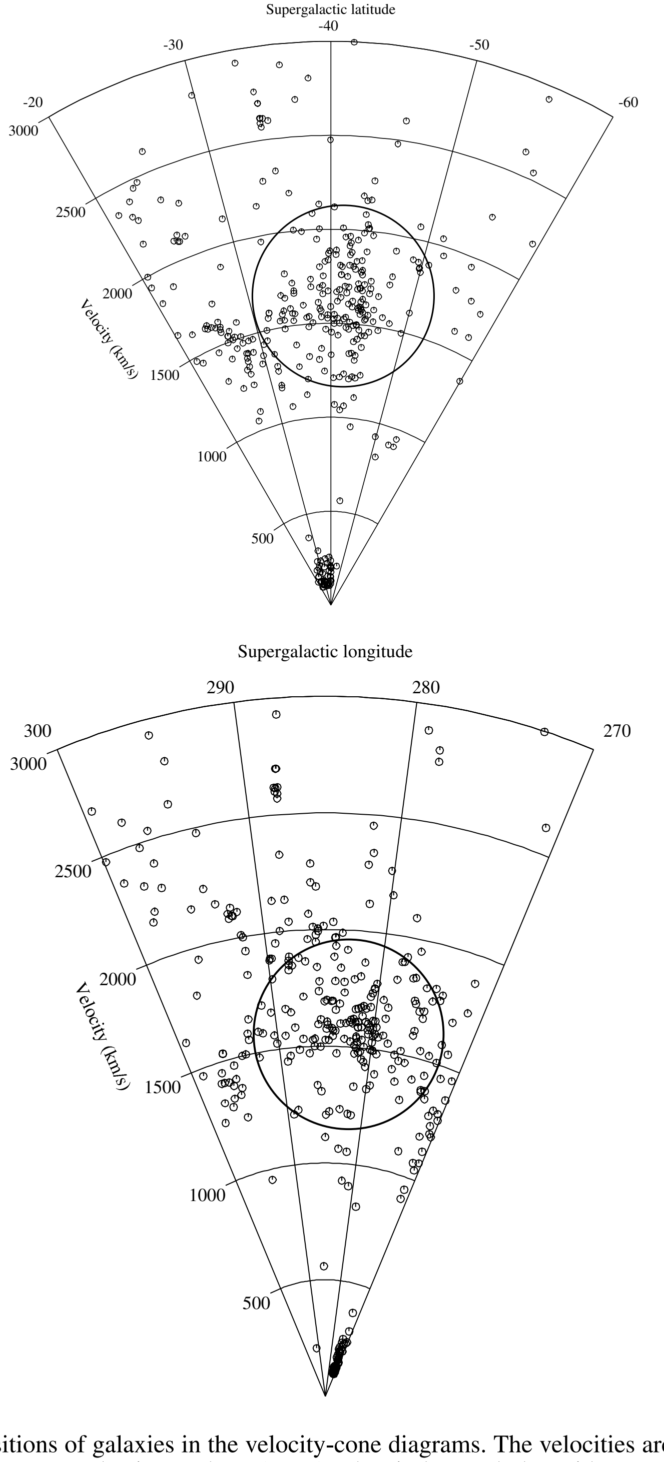

Figure 1. Positions of galaxies in the velocity-cone diagrams. The velocities are Heliocentric from the NASA Extra-galactic Database (NED). The circles mark the Eridanus group.

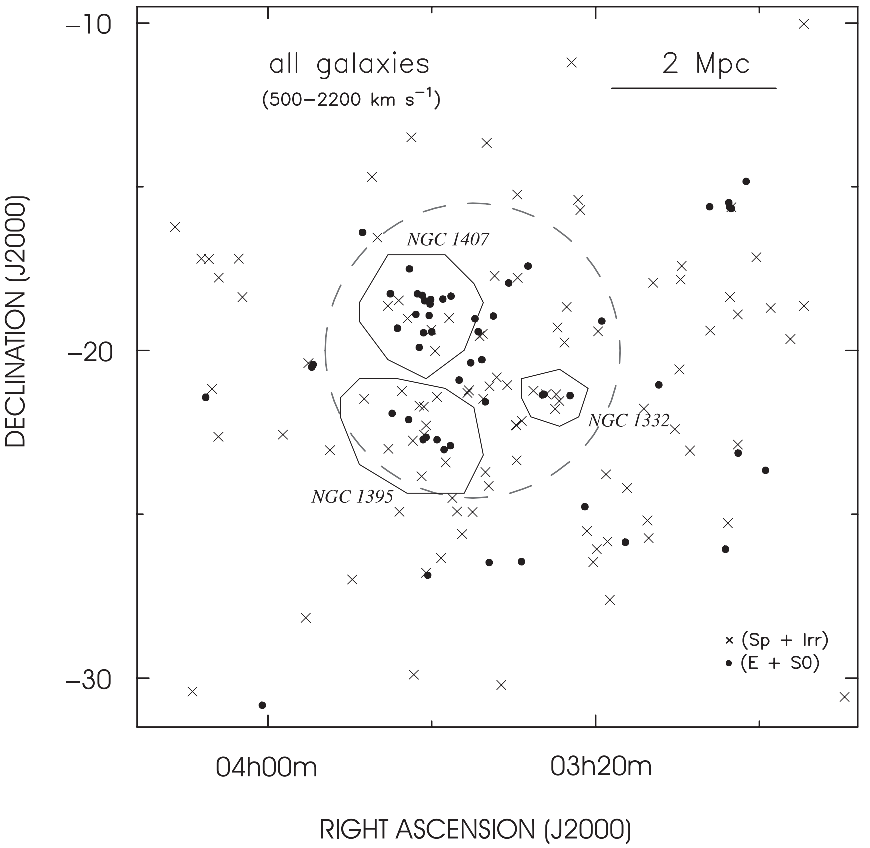

Figure 2. Galaxies in the Eridanus group. The radius of the dashed circle is $\sim$ 2 Mpc within which galaxies were observed with the GMRT. A few sub-groups are marked with their approximate boundaries as identified by Willmer *et al.* (1989).

X-ray emission associated with NGC 1400, NGC 1407 and a few other unresolved sources in the field, diffuse emission centered at NGC 1407 and NGC 1395 can be seen in Fig. 4. The extent of the diffuse emission is $\sim 30'$ ($\sim$ 200 kpc) around NGC 1407 and $\sim 20'$ ($\sim$ 135 kpc) around NGC 1395. No diffuse emission is seen around NGC 1332 (not shown here). Using the PIMMS (Portable, Interactive Multi-Mission Simulator; Mukai 1993) tool, the diffuse emission was modeled as thermal free-free emission from a Raymond-Smith plasma of energy $\sim$ 1.0 keV ($T \sim 10^7$ K) and metallicity 0.2-solar. The choice of the temperature and the metallicity is in accordance with typical values found in X-ray groups (Mulchaey 2000).

The total X-ray luminosity of the diffuse emission in the energy range 0.1–2.0 keV is 1.6×10^{41} erg s^{-1} for the NGC 1407 sub-group and $\sim 6.8 \times 10^{40}$ erg s^{-1} for the NGC 1395 sub-group. The intra-group medium density is estimated as $\sim 2.0 \times 10^{-4}$ cm^{-3} in the X-ray emitting region. The X-ray luminosity of the Eridanus group is about 2–3 orders of magnitude lower compared to that of the clusters like Coma and Virgo. The estimated intra-group medium density is about an order of magnitude lower than that observed in virialised clusters like Coma.

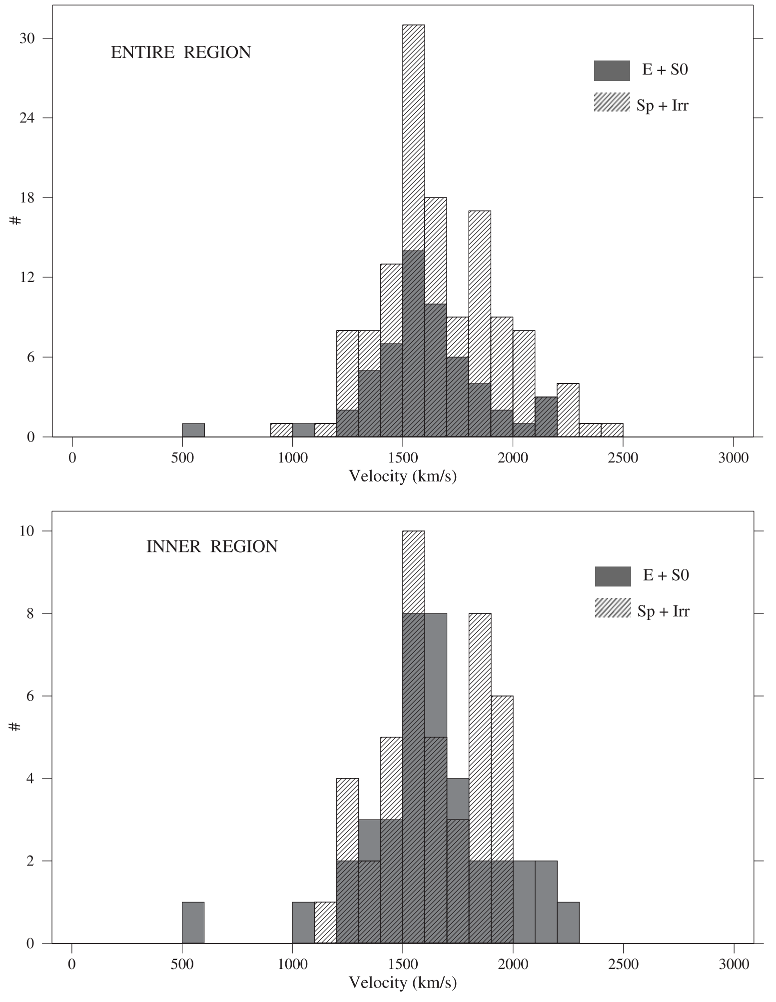

Figure 3. Velocity-histograms of galaxies in the inner 4 Mpc region (bottom panel) and in the entire group (top panel) are shown. There is no appreciable difference in the velocity range over which the early types and the late types are distributed.

2.4 *Comparison of the Eridanus group with other groups and clusters*

The properties of the Eridanus group are compared with the Virgo and the Fornax cluster, and the Ursa-Major group in Table 1. All these systems are at comparable distances. Both the Fornax cluster and the Eridanus group belong to the filamentary structure described by da Costa *et al.* (1988). The Ursa-Major group is a loose group of galaxies (Tully *et al.* 1996). All the four systems have quite different properties. The Fornax cluster having the highest galaxy density has the lowest spiral fraction, consistent with the density–morphology relation. The Eridanus group is intermediate between the Virgo cluster and the Ursa-Major group in terms of its velocity dispersion, its X-ray luminosity, and its number of early-type galaxies. The mean projected galaxy density in Eridanus is intermediate between that in Ursa-Major and in Virgo. The

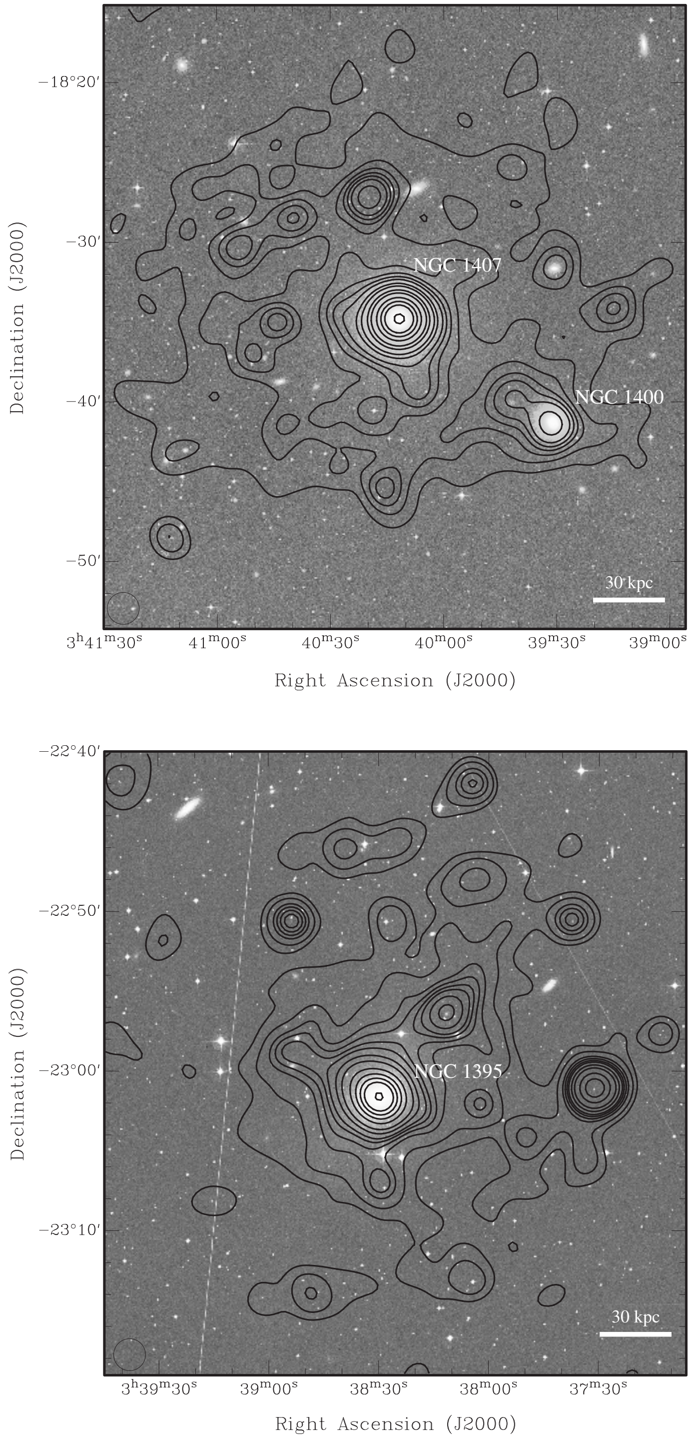

Figure 4. Contours of X-ray emission around NGC 1407 and NGC 1395 overlaid upon the optical images from the DSS. The X-ray images are retrieved from the ROSAT PSPC archived data and smoothed with a circular Gaussian beam of 90".

Table 1. Comparison of four nearby galaxy groups and clusters.

Properties	Virgo[a]	Fornax[b]	Eridanus[c]	Ursa-Major[d]
Distance (Mpc)	17	20	23	21
No. of E + S0s	71	23	36	9
No. of Sp + Irr's	123	17	42	53
(S + Irr) fraction	0.6	0.4	0.5	0.9
Vel. dispersion (km s^{-1})	760	350	240	150
log X-ray luminosity (erg s^{-1})	43.5	41.7	41.4	–
References	1,2,3,4	2,5,6,7	8	9,10

Notes – (**a**): Inner 6° region, (**b**): Inner 2°.4 region, (**c**): Inner 9° region, (**d**): Inner 15° region. **References** – (1) Federspiel *et al.* (1998), (2) Ferguson (1989), (3) Binggeli *et al.* (1987), (4) Mushotzky & Smith (1980), (5) Mould *et al.* (2000), (6) Richter & Sadler (1985), (7) Paolillo *et al.* (2001), (8) Omar (2004), (9) Sakai *et al.* (2000), (10) Tully *et al.* (1996).

galaxies in Virgo are H I deficient. The Ursa-Major group has normal H I content. The X-ray luminosity of the Eridanus group is at the lower end of the X-ray luminosities observed in groups (Mulchaey 2000). The velocity dispersion of the galaxies in the Eridanus group is intermediate between that in Fornax and in Ursa-Major. From this comparison, it appears that the Eridanus group forms a system which is intermediate between a loose group (Ursa-Major) and a rich cluster (Virgo and Fornax).

3. Observations and data reduction

The present GMRT H I observations offer several advantages over studies carried out in the past using single dish telescopes. The GMRT is an interferometric array of thirty 45-m diameter fully steerable parabolic dishes. A description of the GMRT is given by Swarup *et al.* (1991). The GMRT is located at a site (longitude = 74°.05 E, latitude = 19°.092 N, altitude $\sim$ 650 m above MSL) about 80 km north of Pune, India. The configuration of the GMRT is optimized to meet the requirements of high angular resolution and of being able to image extended emission. This optimization is achieved through a hybrid configuration of the antennas. Fourteen of the thirty dishes are located more or less randomly in a compact central array within an area of about 1 $\times$ 1 square kilometer, and the remaining sixteen dishes are spread out along the 3 arms of an approximately Y-shaped configuration over a larger region. The longest separation of antennas is $\sim$ 25 km, and the shortest separation is $\sim$ 100 m. The GMRT is expected to be sensitive to structures on the scales of $2''$–$7'$ at a wavelength of 21 cm. The angular sizes of the galaxies in the Eridanus group are in the range $1'$–$5'$ implying that the data should be sensitive to image radio emission (H I and continuum) over the full extents of galaxies. The FWHM of the primary beam of a GMRT antenna is $\sim 24'$ at 1.4 GHz.

3.1 *Sample of galaxies*

The selection of galaxies for the H I observations were made keeping in mind the broad perspective of the work. The galaxies were not selected based on their H I contents or

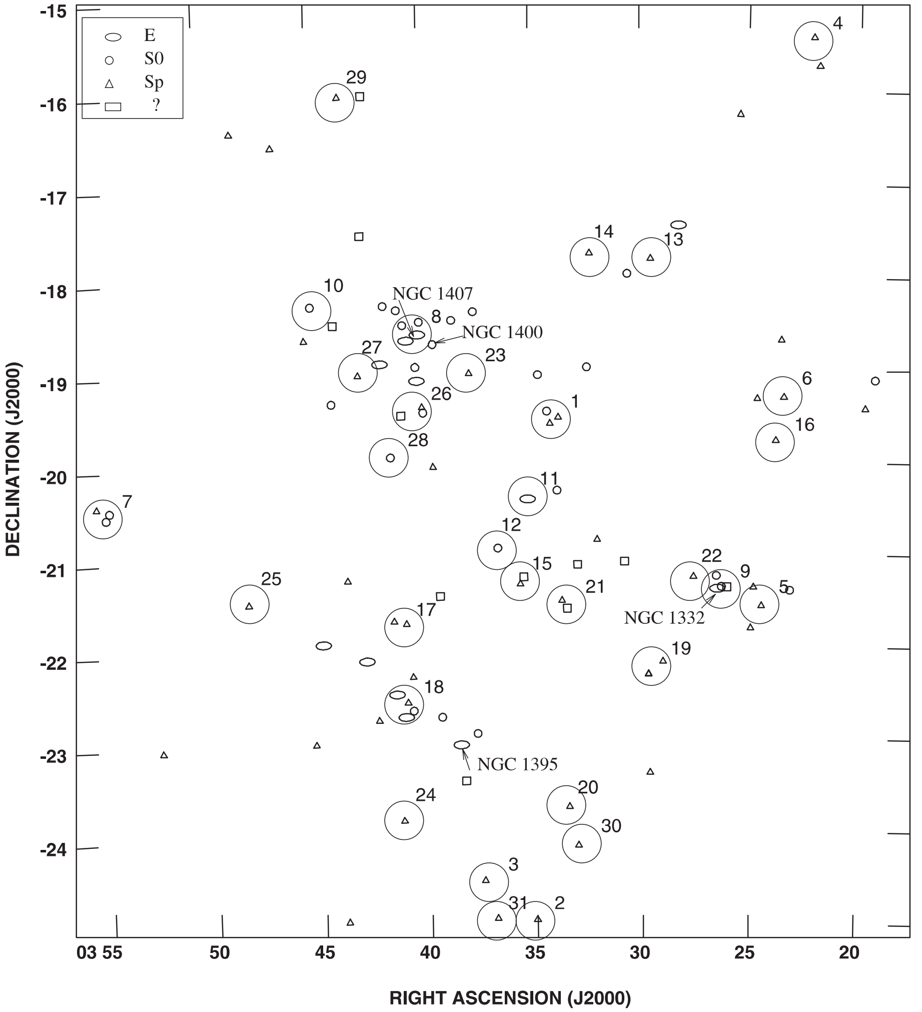

Figure 5. The fields observed with the GMRT. The bigger circles correspond to the FWHM of the GMRT primary beam ($\sim 24'$) at 1.4 GHz.

their optical luminosities. Both early type and late type galaxies were included in the sample. The galaxies were selected from the inner 4 Mpc region of the group where galaxy density is higher and most of the S0s are found. A follow up R-band photometric observations were also carried out with the 1-m optical reflector at the Aryabhatta Research Institute of Observational Sciences (ARIES; *formerly* State Observatory), Nainital. The optical data analysis is presented in Omar (2004).

Since the present H I study with the GMRT was carried out with a limited telescope time of $\sim$ 200 h, the pointing centres of the observations were adjusted in a way to include two or more galaxies within the FWHM of the primary beam. Unfortunately, one complete run of observations on 16 galaxies (during November 2001), mostly early types, was badly affected due to ionospheric scintillations, perhaps related to the intense solar activities during that year. The data collected during this period could not be used to obtain images. Five galaxies from these lost observations were re-observed later in 2002. The science quality data were obtained for a total of 46 galaxies. In Tables 2 and 3, the complete observed sample of 57 galaxies is listed with some of their previously known optical and radio properties.

3.2 *Observational parameters*

The Eridanus group can be observed with the GMRT for $\sim$ 8 h in a given day. Often, two galaxies were observed in each day. The observing strategy was optimized to get uniform distribution of visibilities. Two galaxies were observed alternately for 15–20 min each followed by 5–7 min of observations of secondary calibrators. This cycle was repeated and a total of 3–4 h of observing time was accumulated on each galaxy. Most of the observations were carried out using an 8 MHz bandwidth over 128 channels, which gives a velocity resolution of $\sim$ 13.4 km s^{-1}. The observations were carried out for longer duration ($\sim$ 8 h) for some of the early type galaxies, and with smaller bandwidths (2–4 MHz) for smaller inclination galaxies to get sufficient velocity resolution. A total of $\sim$ 200 h of the GMRT observations were carried out spread over 3 years (2000–2002). The data obtained during November 2001 which were corrupted due to scintillations were discarded. The observing parameters are listed in Table 4.

The VLA calibrators 0240-231 and 0409-179 were used as the secondary calibrators. 0240-231 is classified as "un-resolved" for all the four VLA configurations with a 20-cm flux density of 6.3 Jy. 0409-179 is resolved by baselines longer than 10 km with a 20-cm flux density of 2.2 Jy. 0137 + 331 (3C 48) and 0542 + 498 (3C 147) were used as the primary calibrators. 3C 48 is resolved by baselines longer than 8 km with a 20-cm flux density of 16.5 Jy and 3C 147 is resolved by baselines longer than 10 km with a 20-cm flux density of 22.5 Jy. 3C 48 was observed in the beginning and 3C 147 was observed at the end of each observing run for 20–30 min. The flux densities of the primary calibrators were estimated at the observed frequencies using their known radio spectra from the VLA observations in the 1999.2 epoch.

3.3 *Data acquisition and reduction*

The data (visibilities) were collected in the LTA (Long Time Accumulation) format, which is the native format for the GMRT data. The LTA data were converted to FITS (Flexible Image Transport System) format for subsequent processing. Visibilities were averaged over $\sim$16 s. The data were monitored online. The data were later flagged from the antennas having low gains, for time ranges where data were corrupt, and at lower elevations (usually below 25°) where correlation drops significantly (below 50% in some cases). The flux densities of the secondary calibrators were estimated based on the flux densities of the primary calibrators. The visibilities on the target galaxies were calibrated by interpolating the complex gains determined using the secondary calibrators. Since the spectral responses of filters are not flat, the initial calibration was carried out using the data averaged over four to six channels. The spectral response of the antennas were determined using both the secondary and the primary calibrators, and an averaged spectrum was used to correct the band shapes. The gains start declining significantly after the 110th channel. The first 1–3 channels are generally corrupted in the filter response. Therefore, the data were used between channels 3 and 115. An initial Hɪ spectrum was generated using the AIPS (Astronomical Image Processing System) task POSSM at spatial frequencies below 2 kλ in the direction of target galaxies. This range of spatial frequencies enables most of the H I signals to be detected in the H I spectrum. This spectrum is to identify channels with H I emission.

The continuum-data were generated by averaging the channels devoid of H I line emission. The continuum images were made using this channel averaged data and were used for self-calibration. Several iterations of phase self-calibrations were performed to improve the dynamic range of the images. The final self-calibrated solutions were applied to the line-data. The continuum emission was subtracted from the line-data using the AIPS tasks UVSUB and UVLIN. The self-calibrated and continuum subtracted line-data were used to make the image cubes at different resolutions by selecting appropriate (u, v) ranges. The image cubes were made at two resolutions – one with a resolution of $\sim 15''$ (high resolution cube) using (u, v) data in the range 0.2–20 kλ, and another with a resolution of $\sim 50''$ (low resolution cube) using (u, v) data in the range 0.2–5 kλ.

4. Image analysis

The images were analysed using the GIPSY (Groningen Image Processing System) package developed by the Kapteyn Institute, the KARMA visualization tool (Gooch 1996), and the AIPS package developed by the National Radio Astronomy Observatory.

Since the angular resolution varied by a few arc second in different cubes, all high resolution cubes were convolved to a common resolution of $20'' \times 20''$. In some cases, intermediate resolution cubes at $25''$ or $30''$ were also made. The channel images typically have an rms of 1 mJy beam^{-1}. The 3σ column density detection limit in the $20''$ images is 1×10^{20} cm^{-2}. The cubes are sensitive (3σ) to detect a galaxy of H I mass 1.2×10^7 M$_\odot$ for an H I line-width of 50 km s^{-1}. The image cubes were inspected visually to identify H I signals. The channel images are presented for all the H I detected galaxies elsewhere (Omar 2004). An example of the channel images is shown in Fig. 6.

4.1 *Total H I map and H I diameter*

The zeroth and the first order moment maps were generated at both the low ($50''$) and the high ($20''$) angular resolutions. The moment zero map or the total H I image is obtained by summing the H I images in different channels. The cubes were first blanked to separate the H I signals from noise before summing the channels. The blanking can be done in several ways. The total H I image depends on the blanking procedure (Rupen 1999). One of the methods is to blank the pixels below a certain flux density level. A higher cutoff (e.g., 5σ) makes the total H I images patchy while a lower cutoff (e.g., 3σ) makes the images noisy. The low surface brightness nature of H I emission makes it difficult to separate the low level signals from noise. A hybrid approach has been shown to be effective in overcoming this problem (Rupen 1999). This approach involves masking the noise after smoothing the cube using the AIPS task MOMNT. The moment maps are still estimated using the un-smoothed cube in this approach.

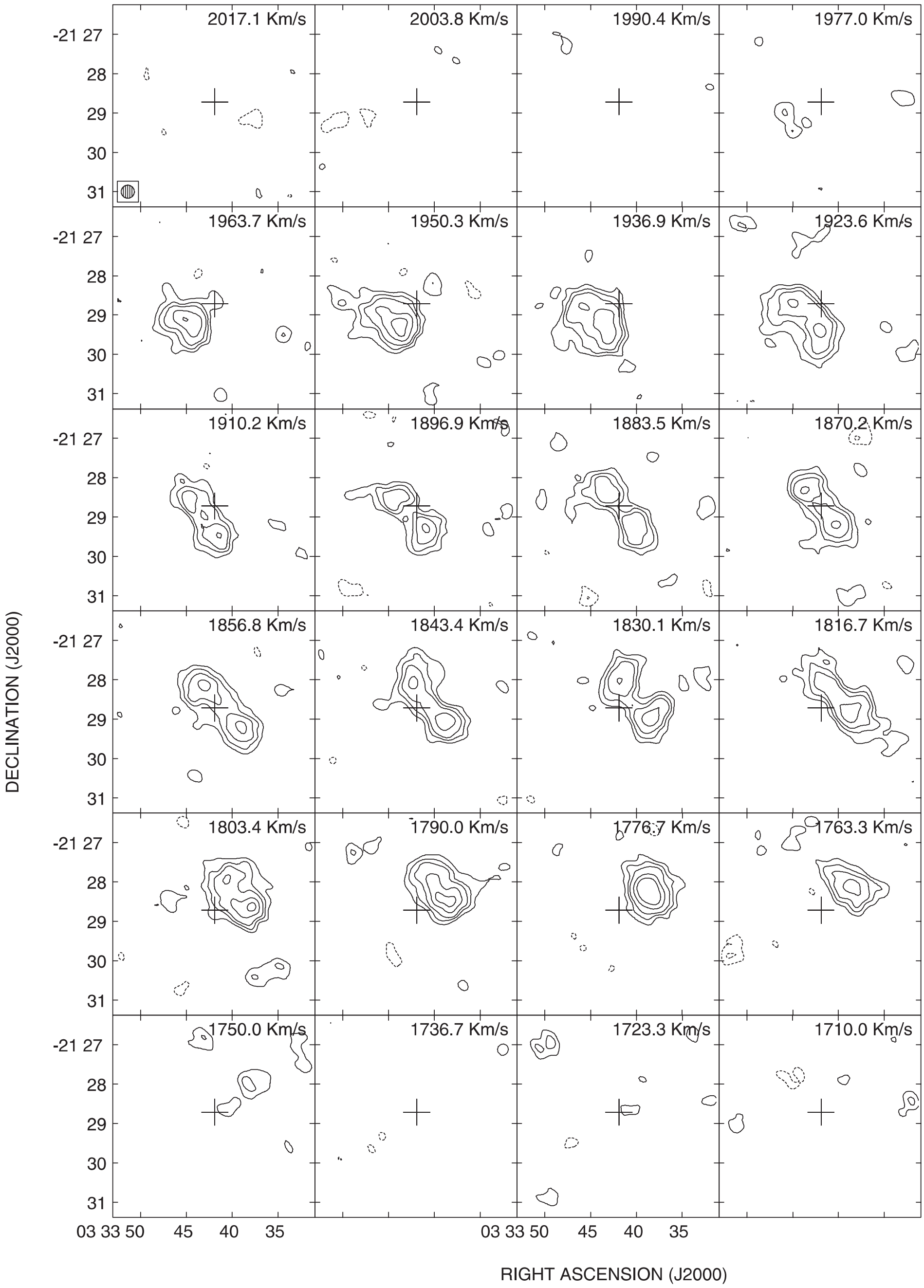

Figure 6. H I emission from IC 1953. The '+' sign marks the optical centre of the galaxy. The rms/channel is 1.4 mJy beam^{-1}. The contours are at 2.5, 3.75, 5, 7.5, and 10 times the rms. The images are convolved with a circular Gaussian beam of $20'' \times 20''$.

The flux density (mJy beam^{-1}) is converted to H I column density using the following relation (equation 3.38, Spitzer 1978):

$$N_{\text{H I}}(\alpha, \delta) = \frac{1.1 \times 10^{21}\,\text{cm}^{-2}}{\theta_a \times \theta_b} \delta v \sum_{j=1}^{N_{\text{chan}}} S_j(\alpha, \delta), \quad (1)$$

where θ_a and θ_b are the FWHM of the synthesised beam measured in arc second along the major and minor axes respectively. S_j is the H I flux density (mJy beam^{-1}) in the channel j and δv is the velocity resolution in km s^{-1}. The H I gas is assumed to be optically thin. A collage of the integrated H I maps of the Eridanus galaxies is shown in Fig. 7 as contours and in Fig. 8 as colour-coded. The individual galaxies are enlarged ten times. To avoid overlap, some galaxies are slightly displaced from their actual positions.

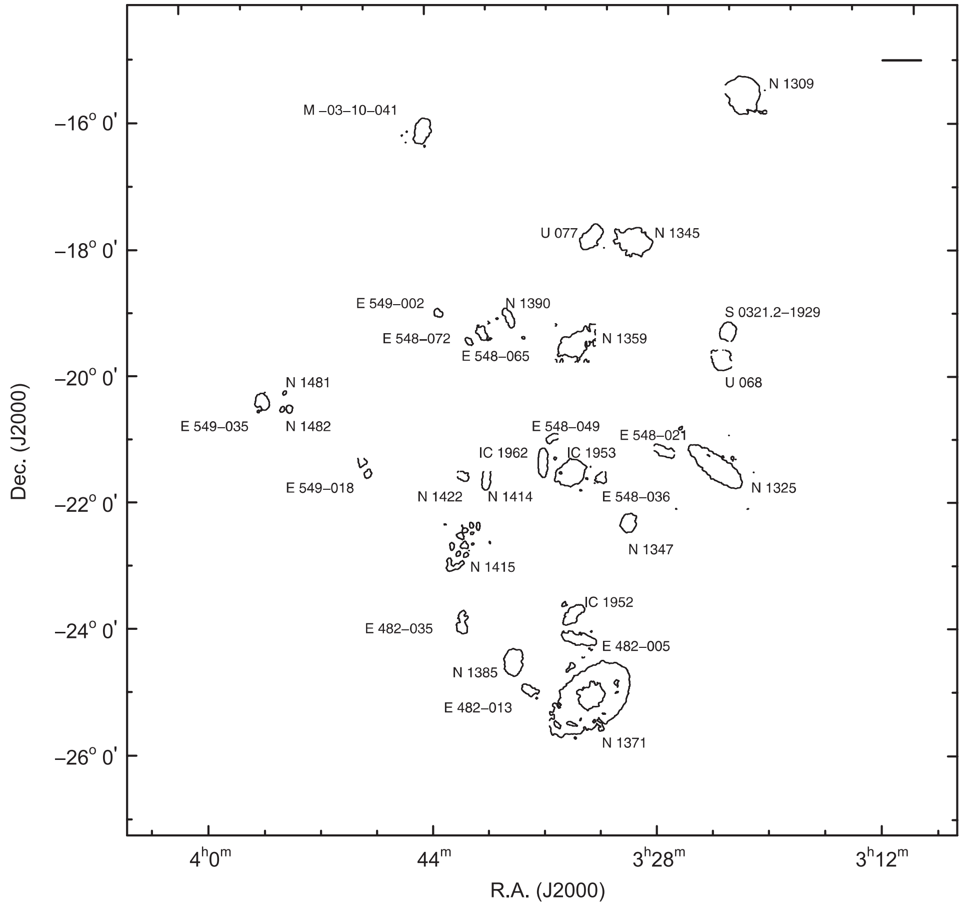

Figure 7. A contour-image collage of the H I detected galaxies in the Eridanus group. Only one contour is plotted to indicate the extent of each galaxy at $N_{\text{H I}} = 10^{20}\,\text{cm}^{-2}$. The individual galaxies are magnified ten times. To avoid overlap, some galaxies are slightly displaced from their actual positions. A bar at the upper right hand corner indicates a scale of 20 kpc for the enlarged sizes of the galaxies. Otherwise, 1° corresponds to ~ 400 kpc.

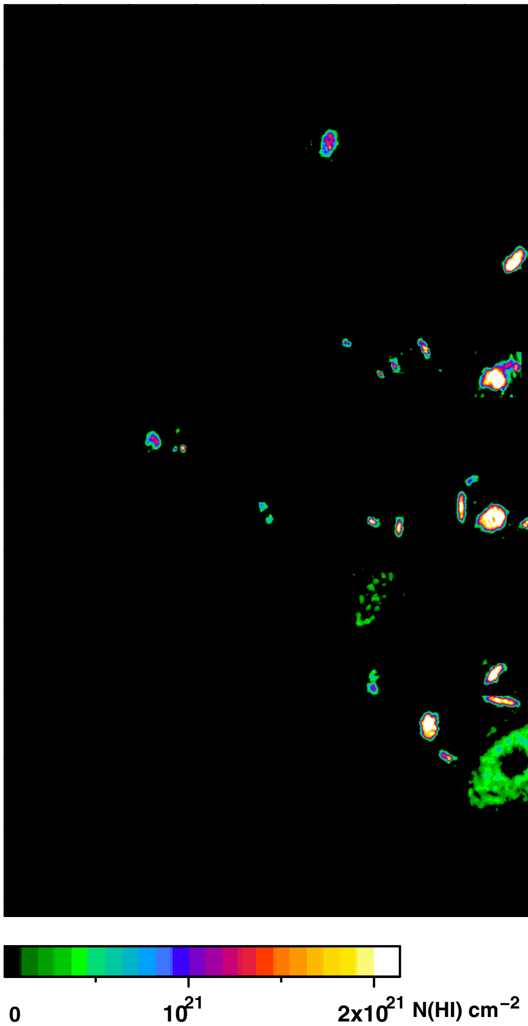

Figure 8. A collage of the HI detected galaxies in the Eridanus group. The colour key indicates the HI column density.

The diameters of the HI disks were estimated from the high resolution total HI images at a fixed face-on HI surface density of 1 $M_\odot$ pc^{-2}. Due to projection effects, the sensitivities to the face-on HI surface densities were not uniform. Therefore, in some cases the HI diameters were extrapolated to the face-on HI surface density level of 1 $M_\odot$ pc^{-2}.

4.2 *HI velocity field*

The conventional way of deriving the velocity field is to compute the intensity-weighted first order moment of the HI images at different velocities. There is an alternative to obtain velocity fields by fitting the HI profiles at every pixel with a Gaussian. These profiles are usually asymmetric depending upon the kinematics of HI along the line-of-sight, and also due to the beam smearing caused by the finite size of the synthesised beam. The broadening and the asymmetry will depend upon the HI distribution in the galaxy. The effect of beam smearing will be more pronounced in edge-on systems. As a result of the asymmetry and the broadening in the HI profile, a single Gaussian component will not give an accurate result. Unfortunately, multi-component Gaussian fit could not be carried out as the signal-to-noise ratio of the detections were not sufficient.

Rupen (1999) has briefly discussed the merits and drawbacks of these two procedures. In the present analysis, the first order moment maps were found to be generally noisier than the velocity field maps obtained by Gaussian fits. This may be because the Gaussian fits were not as sensitive to the outliers as moment maps were. Therefore, in the present analysis, Gaussian fits were used to construct the velocity field maps. It should be noted that both the procedures to obtain the velocity field will underestimate rotation velocities at locations of steep velocity gradients. The flat part of the rotation curve, however, remains unaffected.

4.3 *Global HI profiles*

The integrated HI flux density as a function of velocity is the global HI profile as would have been obtained from a single dish observation. The low resolution (50″) cubes were used to obtain the global profiles as these cubes are most sensitive to the diffuse emission. The lower resolution zeroth order moment map was used to mark the region over which the flux density was estimated in the channel images. The HI mass is obtained by using the following relation:

$$M_{\rm HI}\,({\rm M}_\odot) = 2.36 \times 10^5 D^2\, \delta v \sum_{j=1}^{N_{\rm chan}} S_j \quad (2)$$

where D is the distance in Mpc, S_j is the integrated flux in Jy in the spectral channel j of velocity width δv in km s^{-1}. The distance is taken as 23 Mpc. In Fig. 9, the integrated HI flux ($\delta v \sum_{j=1}^{N_{\rm chan}} S_j$) from the GMRT is compared with that from the HIPASS data and from other single dish data. Some of the galaxies with higher values of the integrated HI flux in the single dish data show significantly less flux in the GMRT. The HI disk sizes of these galaxies are among the largest ($> 6'$) in our sample. We believe that the loss of flux for the large galaxies in the GMRT images is due to inadequate sampling of shorter (u, v) spacings in the GMRT.

4.4 *HI line-width*

The HI global profiles often peak at the two extreme ends of the rotation velocities of galaxies. The detailed shape of an HI profile depends on the rotation curve, the inclination and the HI distribution in the galaxy. The HI line-widths are broadened from their true values due to random motions in the HI gas and due to the finite spectral resolution. The HI line-width is a crucial parameter for studying the Tully–Fisher (TF) relation. Most of the TF studies still use the HI line-widths obtained from single dish observations because of the simplicity of such observations. The synthesis data of the Eridanus group of galaxies provide an opportunity to compare the corrected HI

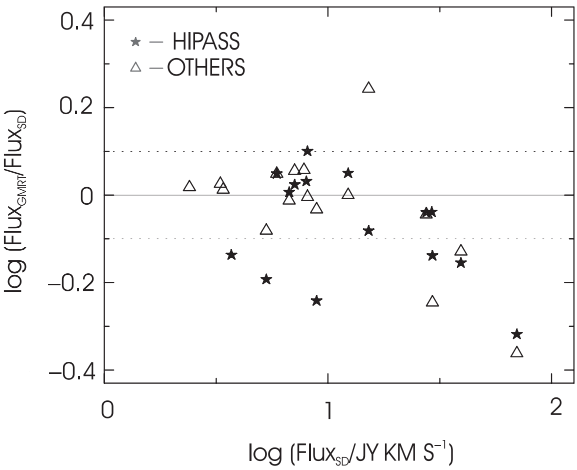

Figure 9. A comparison of the integrated HI flux densities of Eridanus galaxies from the GMRT with those from the single dish data published elsewhere and from the HIPASS. Most of the ratios are within ±25% of unity (indicated by the dotted lines).

line-widths obtained from the single dish HI profiles with those obtained from the HI rotation curves.

For those cases in which double-peaked HI profiles are seen, HI line-widths were estimated at 20% (W_{20}) and at 50% (W_{50}) levels of the peak intensities at the two ends of the HI profiles. The locations of the two peak intensities were estimated separately using Gaussian fits to the profiles. Bottinelli *et al.* (1990) derived an empirical relation to correct for the instrumental broadening. They convolved the HI profile progressively with coarser velocity resolutions for a model galaxy, and determined the broadening. A linear relationship between the channel resolution and the instrumental broadening was suggested. The broadening correction is estimated as $\delta W = 0.55 \times \delta V_i$ for W_{20} and $\delta W = 0.13 \times \delta V_i$ for W_{50} for an instrumental resolution of δV_i. For the current observations, $\delta V_i = 13$ km s^{-1}, implying that the corrections are ~ 7 km s^{-1} for W_{20} and ~ 2 km s^{-1} for W_{50}.

A linear summation of the rotation velocity and the random velocity is appropriate to estimate the observed width for the cases where the intrinsic width is almost boxy (i.e., in fast rotating galaxies). However, a summation in quadrature will be required for the slow rotating (e.g., dwarf) galaxies where the solid body rotation together with the radial distribution of the HI gas will lead to an almost Gaussian profile. A composite relation for all galaxies was given by Tully & Fouque (1985). According to their relation, the width due to the rotation motion W_R, the width due to random and turbulent motions W_t, and the observed width W_l are related by:

$$W_l^2 = W_{R,l}^2 - W_{t,l}^2 \left(1 - 2e^{-(W_l/W_{c,l})^2}\right) + 2W_l W_{t,l} \left(1 - e^{-(W_l/W_{c,l})^2}\right), \qquad (3)$$

where the subscript l refers to the level (20%, or 50%) at which the widths are estimated. The $W_{t,l}$ is estimated as $2k_l\sigma$ from the velocity dispersion of the HI gas (σ) due to random and turbulent motions. The constant factor k_l is 1.80 at 20% level and

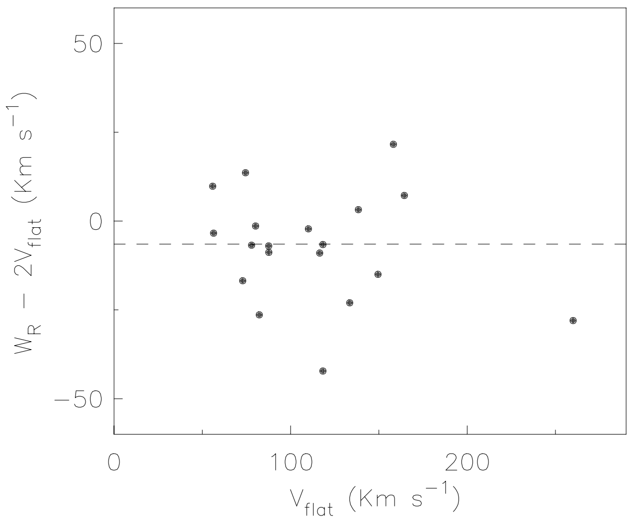

Figure 10. Comparison of the corrected HI widths ($W_{R;50}$) with the flat rotation velocities of the Eridanus galaxies. The dashed line is the mean value at 6.5 km s^{-1}.

1.18 for the 50% level for a Gaussian profile. The value of σ is taken as 6 km s^{-1}. $W_{c,l}$ is a parameter which defines the transition region from linear to quadratic sum. The equation (3) does a linear subtraction if $W_l > W_{c,l}$ and a quadratic subtraction if $W_l < W_{c,l}$. The values of $W_{c,l}$ are determined empirically as 120 km s^{-1} for the 20% level and 100 km s^{-1} for the 50% level by Tully & Fouque (1985).

The corrected HI widths are compared with the flat rotation velocities of the galaxies in Fig. 10. The mean value of the difference ($W_{R,50} - 2V_{\rm flat}$) is $\sim$ 6.5 km s^{-1}.

4.5 *Rotation curves*

The rotation curves were derived using the tilted ring model (cf. Begeman 1989). The GIPSY task ROTCUR was used. The basic methodology of this model is the following. The model assumes the gas to be in circular orbits. The position angle and the inclination of the HI disk are allowed to vary with radius. The fitting procedure generally involves estimation of 5 unknowns, *viz*., the dynamical centre (X,Y), the systemic velocity ($V_{\rm sys}$), the position angle (PA) of the major axis, the inclination angle (INCL), the circular rotation velocity ($V_{\rm rot}$), and optionally the expansion velocity $V_{\rm exp}$. The observed radial velocity $V(x, y)$ at a rectangular sky coordinate (x, y) and at a radius r is given by:

$$V(x, y) = V_{\rm sys} + V_{\rm rot}\cos(\theta)\sin(INCL) + V_{\rm exp}\sin(\theta)\sin(INCL), \quad (4)$$

where

$$\cos(\theta) = \frac{-(x - X)\sin(PA) + (y - Y)\cos(PA)}{r}, \quad (5)$$

$$\sin(\theta) = \frac{-(x - X)\cos(PA) + (y - Y)\sin(PA)}{r\cos(INCL)}. \quad (6)$$

The V_{exp} term was not fitted in the present analysis, and was kept fixed at zero. V_{exp} can be used to estimate the non-axisymmetry in the velocity field. The velocity fields at 20″ resolution obtained via Gaussian fits were used in this analysis. The iterative procedure described by Begeman (1989) is used to estimate the disk's kinematical parameters and the rotation curve. The velocities are averaged in elliptical annuli of width 10″ and extracted as a function of the azimuth at different radii in increments of 10″. The velocity fields in the receding side and in the approaching side were fitted separately to obtain two rotation curves. The iterative scheme to estimate the different parameters is described below.

4.5.1 *Dynamical centre (X,Y) and systemic velocity (V_{sys})*

The velocity determined from the H I width or the optical velocity of the galaxy was used as the initial guess for the systemic velocity. The guesses for the centre, the position angle and the inclination angle were their respective estimates obtained from the ellipse fits to the optical isophotes. The first iteration is started by fixing the inclination and the position angle, and fitting the centre and the systemic velocity. If the velocity field is symmetric, the fitted values of the dynamical centre and the systemic velocity should be similar for all the rings. However, often galaxies do not have symmetric velocity fields due to kinematical lopsidedness. Therefore, slightly different estimates of centre and systemic velocity may result from each ring. An overlay of the velocity field contours over the optical image helps in deciding the quality of the fit. For a galaxy with no warp, the velocity field lines should run straight along the minor axis. The line joining the cusps of the iso-velocity contours of identical rotation velocity at the two halves of the galaxy should trace the direction of the major axis. The intercept of the major axis with the minor axis is expected to be the dynamical centre.

If a galaxy has a warp, the velocity field lines will show a characteristic integral sign shaped structure. Often by a visual inspection of the velocity field, it was possible to decide whether reasonably good fits were obtained or not. It was found in some cases that the dynamical centre was not coincident with the optical centre (e.g., in IC 1953). The centre and the systemic velocity were computed as un-weighted mean of their values in all the rings for which satisfactory solutions could be obtained. Once the centre and the systemic velocity are determined, these values are held fixed for all radii during successive iterations.

4.5.2 *Position angle*

In this step, the position angle is determined as a function of radius. The inclination angle for each radius is kept fixed and V_{rot} is allowed to vary. The variations in position angle with radii can be inferred from a visual inspection of the velocity field. If a galaxy is warped, the position angle varies gradually starting at certain radii and often becomes constant at large radii. A warp often results in variations in both the inclination and the position angle simultaneously. For galaxies, where no significant change in the position angle or in the inclination or in both were seen, an average value of the position angle was taken.

4.5.3 *Inclination*

In this iteration, the variations in the inclination angle are modeled as a function of radius. The previously determined parameters (centre, systemic velocity, and PA) are kept fixed. Reliable estimates for the inclination can not be made for galaxies having low inclination (usually below 45°), using the tilted ring model (Begeman 1989). In such cases, optical inclination angles are more reliable.

4.5.4 *Rotation velocities*

In the final iteration, all the disk parameters obtained from the previous iterations are kept fixed, and a fit is carried out to obtain the circular rotation velocity as a function of radius. The receding and the approaching sides of the galaxies were fitted separately. In this step, a cosine weighting scheme was adopted such that points along the major axis have maximum weight and points along the minor axis have zero weight. In addition, points within ± 20 degree from the minor axis were excluded. This is due to the fact that the minor axis does not have any information on the rotation velocity, and the points along the major axis give a direct estimate of the projected rotation velocity.

The rotation velocities obtained from the tilted ring fit should be corrected for the effects of beam smearing. The effects of beam smearing are maximum at the locations of steep velocity gradients. The flat portion of the rotation curve remains nearly unaffected due to beam smearing. The rotation curves presented here are not corrected for the effects of beam smearing. Therefore, for those analyses which are critically dependent on the quality of the rotation curves (e.g., mass modeling), these rotation curves should not be used without making an appropriate correction. Such analyses will be presented elsewhere.

4.6 *Radial H*I *density profiles*

The total HI maps were used to estimate the mean radial HI surface density profiles by azimuthally averaging the HI column densities in concentric elliptical annuli. The axial parameters of the ellipses were obtained from the tilted ring models. The elliptical annuli were sampled at intervals of $10''$ to get two points in one synthesised beam of $20''$. The widths of the annuli were kept fixed at $10''$. The average radial profile in each annulus is scaled by the ratio of the total HI mass to the summed column density in all annuli to obtain the HI mass surface density. The profiles are corrected for the projection effects to obtain the face-on mass surface density in units of $M_\odot$ pc^{-2}. The profiles can be quite uncertain in high inclination galaxies where some flux density from the lower radii along the minor axis will be included at larger radii due to finite spatial resolution. Also, the profiles will artificially extend to larger radii near the outer edge of the HI disk due to the finite angular resolution.

4.7 *Dynamical mass*

The dynamical mass can be estimated from the rotation curves. The total mass within a radius R (kpc) can be derived using the relation $M_{\rm tot}(M_\odot) = 2.3 \times 10^5 V_{\rm rot}^2 R/G$, where V_{rot} is the rotation velocity in km s^{-1}. There can be several choices for the radius R, e.g., H I disk radius, optical disk radius, disk scale length, etc. The dynamical masses were estimated within the optical radius (i.e., $D_{25}/2$) in the present analysis. The estimates were made only for those galaxies in which flat rotation curves were detected.

5. H I properties of galaxies

In this section, some of the H I properties of galaxies derived from the GMRT observations are presented and are compared with those for nearby galaxies in field and in other loose groups.

5.1 *H I and total dynamical mass*

The histogram of H I masses of galaxies detected by GMRT is shown in Fig. 11. The lowest H I mass ($\sim 8 \times 10^8$ $M_\odot$) detected is that of an S0 galaxy NGC 1481. Some galaxies towards the high mass end in the histogram will have their H I masses underestimated by GMRT. Due to the limited sample size, this plot is of limited statistical significance to estimate the H I mass function.

The dynamical masses are plotted in Fig. 12 as a function of Hubble type. Only those galaxies are plotted whose flat part of the rotation curve could be measured. There seems to be a systematic trend in the sense that early type galaxies have on average higher dynamical masses than the late type galaxies. This result is consistent with other studies (e.g., Broeils & Rhee 1997; Verheijen & Sancisi 2001).

The statistical significance of the correlation was estimated using the Spearman Rank-Order Correlation Coefficient method. The significance of the non-zero correlation coefficient in Fig. 12 is $\sim 97\%$.

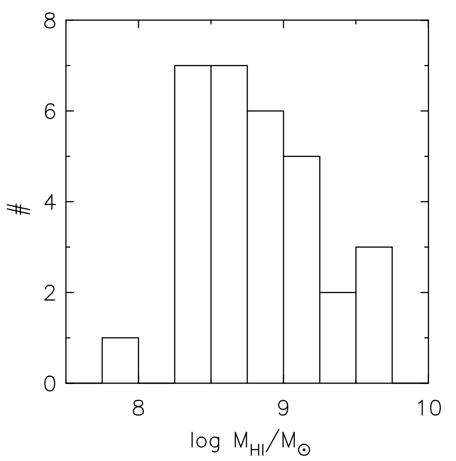

Figure 11. The histogram of H I masses of the Eridanus galaxies observed with the GMRT.

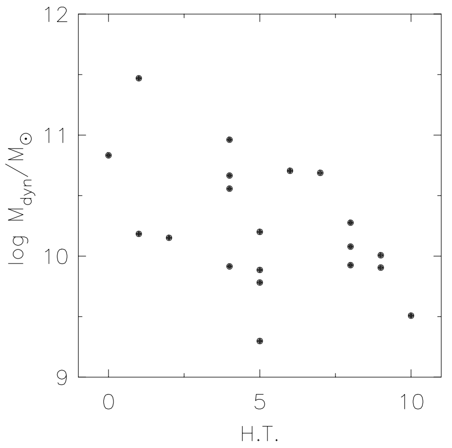

Figure 12. Dynamical mass plotted against the Hubble type. The masses are estimated within the optical diameter (D_{25}).

5.2 *H*I *mass to luminosity ratio*

The ratio of the HI mass to the luminosities in the B, R, J, and K bands are plotted in the different panels of Fig. 13 respectively against the Hubble types. The B-band luminosities are estimated using the face-on magnitudes from the RC3 catalog, and assuming the Sun's absolute magnitude in the B-band to be 5.48. The values of M_{HI}/L_B are in general consistent with that of Broeils & Rhee (1997). No significant trend in the M_{HI}/L ratio with respect to the type is seen in the B-band. The significance of any correlation is less than $\sim 70\%$.

However, significantly higher probabilities ($> 97\%$) were found for a correlation between M_{HI}/L and H.T. in the other bands. The correlations in the R and the near-IR (J & K) bands are in the sense that late type galaxies have on an average higher M_{HI}/L value. This trend in M_{HI}/L in the J and K bands for which the extinction corrections are relatively less significant are consistent with the results for the Ursa-Major galaxies (Verheijen & Sancisi 2001).

5.3 *Ratio of H*I *diameter to optical diameter*

The ratio of the HI diameter to the optical diameter is plotted in Fig. 14 against various properties of the galaxies. No significant correlation is seen with the Hubble type, the HI mass, the projected distance to the nearest neighbour, and the J-band magnitude. Contrary to this, Verheijen & Sancisi (2001) found a significant correlation between D_{HI}/D_{25} and J-band magnitude as well as Hubble type for the Ursa-Major group of galaxies. The average value of D_{HI}/D_{25} is 1.7 ± 0.8, which is consistent with the value of 1.7 ± 0.5 obtained by Broeils & Rhee (1997) for a sample of nearby luminous galaxies.

5.4 *H*I *surface density*

The HI masses of galaxies are observed to correlate with their HI diameters and optical diameters (Haynes & Giovanelli 1984; Broeils & Rhee 1997; Verheijen & Sancisi

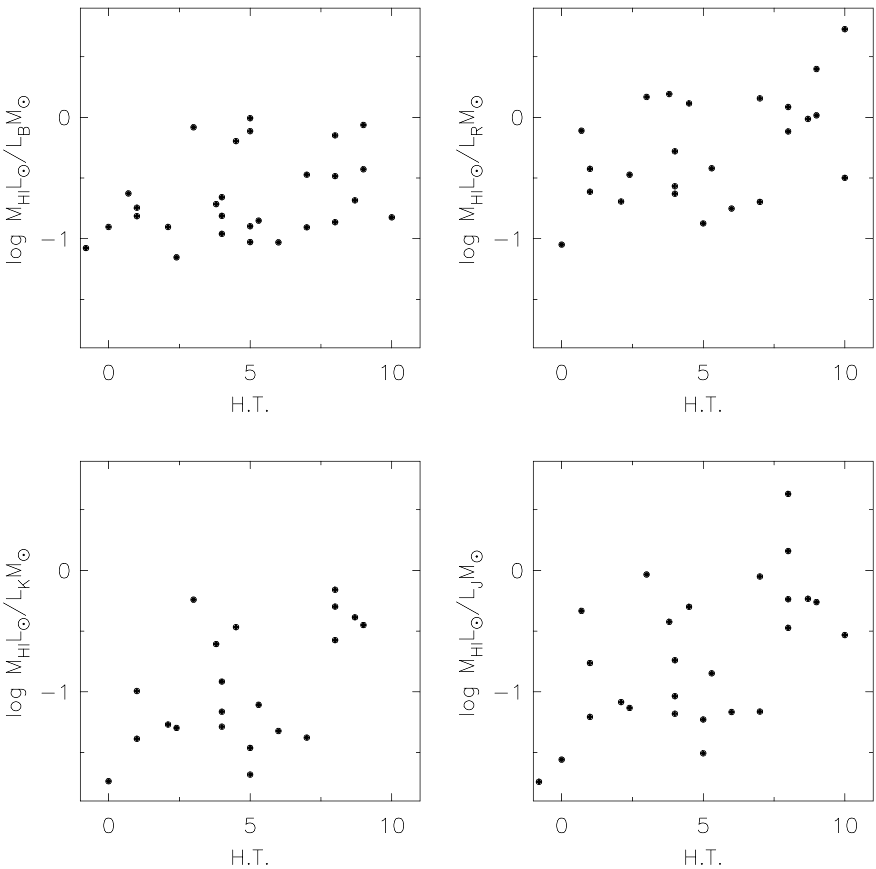

Figure 13. The H I mass to luminosity ratio in the optical and the near-IR bands. There appears to be a trend in the R, and in the near-IR bands in the sense that late type galaxies have on an average higher value of $M_{\rm HI}/L$.

2001). The latter authors showed that the correlation is tighter with the H I diameter than with the optical diameter with a slope of ∼ 2. The lower panel of Fig. 15 shows log $M_{\rm HI}$ for the Eridanus galaxies plotted against log D for both optical and H I diameters. A straight line is fitted with a fixed slope of 2. It can be seen that the H I diameters of the galaxies in the Eridanus group are more tightly correlated than the optical diameters with their H I masses. The upper panel of Fig. 15 shows the distribution of the H I mass surface densities ($\sigma_{\rm HI} = 4M_{\rm HI}/\pi D^2$) of Eridanus galaxies against their Hubble types. It can be seen that the mass surface densities over the H I disks are less scattered compared to the mass surface density over the optical disks.

A summary of the various estimated parameters of the Eridanus galaxies can be found in Table 5.

6. Summary

The Eridanus group of galaxies were observed in the H I 21 cm-line using the GMRT for ∼200 h. There is considerable scope to use this data for several studies which will be presented in subsequent papers. The following conclusions can be drawn from the HI properties of the Eridanus galaxies:

- The early type disk galaxies seem to have higher dynamical masses compared to the late type disk galaxies.
- The $M_{\rm HI}/L$ ratio shows a trend with respect to the type in the R-band and in the near-IR (J & K) bands in the sense that late type galaxies have, on an average, higher $M_{\rm HI}/L$.
- The average value of $D_{\rm HI}/D_{\rm opt}$ is 1.7 ± 0.8 for the Eridanus galaxies is consistent with that for galaxies in other groups and fields.
- The ratio of $M_{\rm HI}/D_{\rm HI}$ has less scatter compared to the ratio of $M_{\rm HI}/D_{\rm opt}$ for different galaxy types.

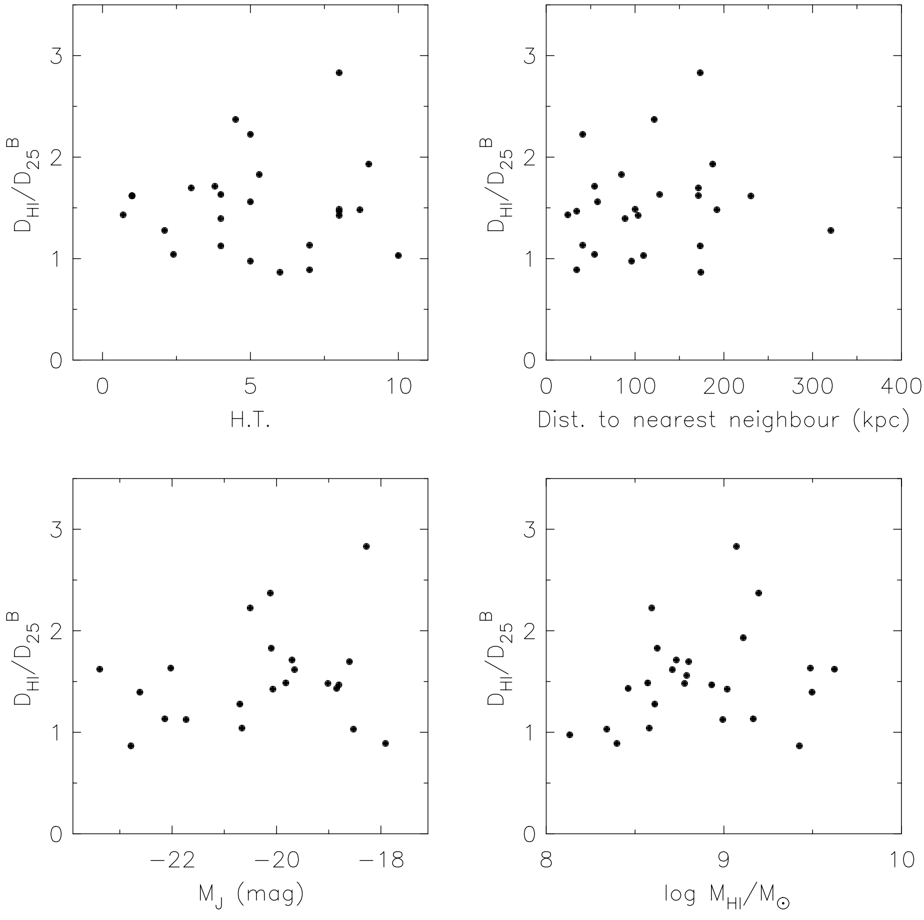

Figure 14. The ratio of the HI diameter to the optical diameter is plotted with different properties of galaxies. The mean ratio of the sample is 1.7 ± 0.8. This ratio is independent of the Hubble type, the HI mass, the distance to the nearest neighbour, and the J-band luminosity.

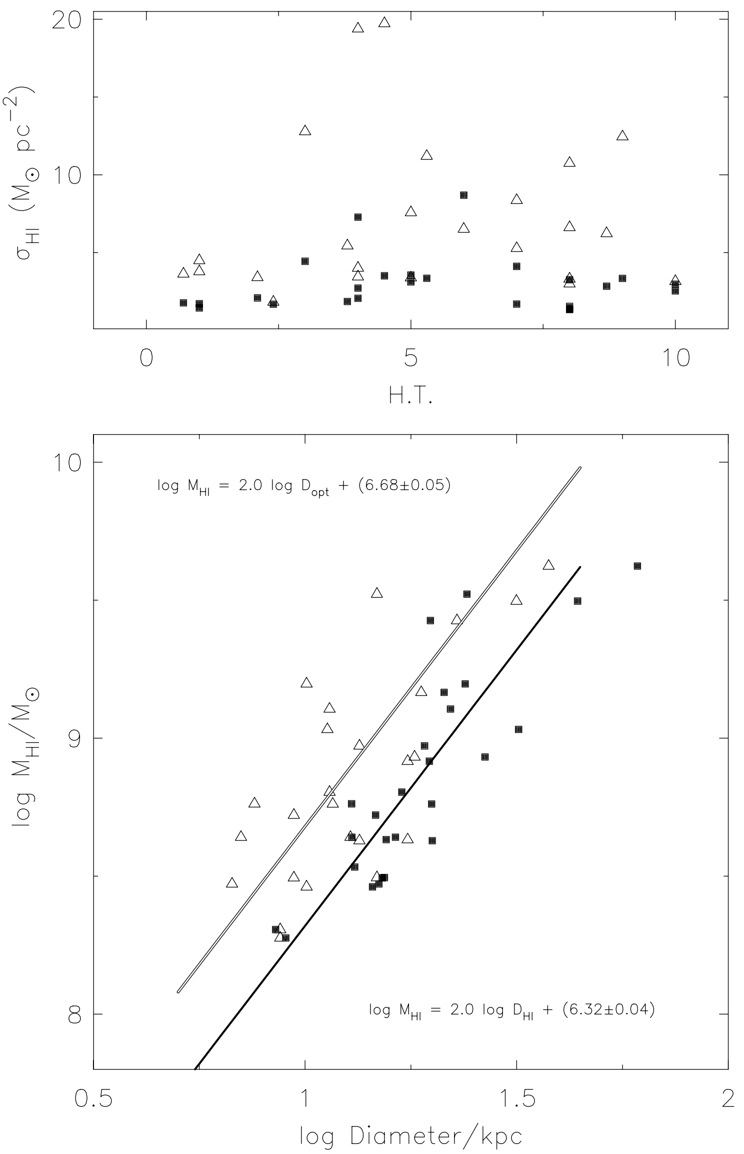

Figure 15. (Lower panel) The HI mass is plotted against HI diameter (filled squares) and optical diameter (open triangles). The two lines are the best fits to the two sets of the data respectively. The slopes were kept fixed at 2. (Upper panel) The HI mass surface density estimated over the HI disk (filled squares) and over the optical disk (open triangles) plotted against the Hubble type.

Acknowledgements

AO would like to acknowledge the encouragement and the support of late K. R. Anantharamaiah in beginning this observational program with the GMRT. We thank Marc Verheijen, Jayaram Chengalur, and the referee for useful comments on various issues discussed here. We thank the staff of the GMRT who made these observations possible. The GMRT is operated by the National Centre for Radio Astrophysics of the Tata Institute of Fundamental Research. This research has been benefited by the NASA's Astrophysics Data System (ADS) and Extra-galactic Database (NED) services. Their open software used in this research is greatly acknowledged.

Appendix A: The Eridanus group of galaxies – optical, infrared and H I properties

Table 2. Sample of galaxies.

#	Name	α(J2000) h	m	s	δ(J2000) $^\circ$	$'$	$''$	l_{SG} $^\circ$	b_{SG} $^\circ$	cz (km/s)
1	NGC 1297	03	19	14.2	−19	06	00	284.30	−38.61	1579
2	NGC 1309	03	22	06.5	−15	24	00	289.12	−38.86	2135
3	NGC 1315	03	23	06.6	−21	22	31	281.46	−39.68	1673
4	SGC 0321.2-1929	03	23	25.1	−19	17	00	284.18	−39.61	1545
5	UGCA 068	03	23	47.2	−19	45	15	283.58	−39.73	1838
6	NGC 1325	03	24	25.4	−21	32	36	281.26	−39.99	1589
7	ESO 548-G 016	03	26	02.4	−21	20	26	281.55	−40.36	2119
8	NGC 1332	03	26	17.3	−21	20	07	281.56	−40.41	1524
9	NGC 1331	03	26	28.3	−21	21	20	281.54	−40.46	1210
10	APMBGC 548 + 070 + 070	03	26	31.3	−21	13	01	281.72	−40.46	1548
11	ESO 548-G 021	03	27	35.3	−21	13	42	281.72	−40.71	1668
12	ESO 548-G 025	03	29	00.7	−22	08	45	280.53	−41.08	1680
13	NGC 1345	03	29	31.7	−17	46	40	286.32	−40.91	1529
14	NGC 1347	03	29	41.8	−22	16	45	280.35	−41.24	1759
15	NGC 1353	03	32	03.0	−20	49	09	282.34	−41.73	1525
16	UGCA 077	03	32	19.2	−17	43	05	286.48	−41.57	1961
17	ESO 482-G 005	03	33	02.2	−24	07	58	277.89	−42.03	1915
18	IC 1952	03	33	26.7	−23	42	46	278.46	−42.13	1812
19	ESO 548-G 036	03	33	27.6	−21	33	53	281.35	−42.09	1480
20	IC 1953	03	33	41.9	−21	28	43	281.47	−42.14	1867
21	NGC 1359	03	33	47.7	−19	29	31	284.15	−42.06	1966
22	ESO 548-G 043	03	34	10.5	−19	33	30	284.07	−42.16	1931
23	ESO 548-G 044	03	34	19.2	−19	25	28	284.25	−42.18	1696
24	NGC 1371	03	35	02.0	−24	55	59	276.80	−42.48	1471
25	NGC 1370	03	35	14.6	−20	22	25	282.99	−42.46	1063
26	ESO 548-G 049	03	35	28.1	−21	13	01	281.85	−42.55	1510

Table 2. *(Continued)*

#	Name	α(J2000) h	m	s	δ(J2000) °	′	″	l_{SG} °	b_{SG} °	cz (km/s)
27	IC 1962	03	35	37.5	−21	17	39	281.74	−42.58	1806
28	NGC 1377	03	36	39.1	−20	54	08	282.29	−42.81	1792
29	ESO 482-G 013	03	36	53.9	−24	54	46	276.82	−42.90	1835
30	NGC 1385	03	37	28.3	−24	30	05	277.38	−43.04	1493
31	NGC 1383	03	37	39.2	−18	20	22	285.80	−42.89	1948
32	NGC 1390	03	37	52.2	−19	00	30	284.89	−42.99	1207
33	NGC 1393	03	38	38.6	−18	25	41	285.70	−43.13	2185
34	NGC 1401	03	39	21.8	−22	43	29	279.81	−43.48	1495
35	ESO 548-G 064	03	40	00.0	−19	25	35	284.36	−43.52	1694
36	ESO 548-G 065	03	40	02.7	−19	22	00	284.45	−43.53	1221
37	IC 0343	03	40	07.1	−18	26	36	285.72	−43.48	1841
38	NGC 1407	03	40	11.9	−18	34	49	285.53	−43.51	1779
39	ESO 482-G 031	03	40	41.5	−22	39	04	279.92	−43.79	1621
40	APMBGC 548-110-078	03	40	52.5	−18	28	29	285.69	−43.66	1595
41	NGC 1415	03	40	56.7	−22	33	47	280.04	−43.85	1585
42	NGC 1414	03	40	57.0	−21	42	47	281.22	−43.84	1681
43	ESO 548-G 072	03	41	00.3	−19	27	19	284.34	−43.76	2034
44	NGC 1416	03	41	02.9	−22	43	09	279.82	−43.87	2167
45	IC 0345	03	41	09.1	−18	18	51	285.92	−43.71	1335
46	ESO 482-G 035	03	41	15.0	−23	50	10	278.27	−43.91	1890
47	NGC 1422	03	41	31.1	−21	40	54	281.27	−43.97	1637
48	IC 0346	03	41	44.6	−18	16	01	286.00	−43.85	2013
49	ESO 549-G 002	03	42	57.3	−19	01	12	284.99	−44.19	1111
50	MCG-03-10-041	03	43	35.5	−16	00	52	289.18	−44.07	1215
51	NGC 1440	03	45	02.9	−18	15	58	286.09	−44.63	1534
52	NGC 1438	03	45	17.2	−23	00	09	279.43	−44.85	1555
53	NGC 1452	03	45	22.3	−18	38	01	285.58	−44.73	1737
54	ESO 549-G 018	03	48	14.1	−21	28	28	281.60	−45.52	1587
55	NGC 1481	03	54	28.9	−20	25	38	283.15	−46.96	1733
56	NGC 1482	03	54	39.3	−20	30	09	283.04	−47.00	1916
57	ESO 549-G 035	03	55	04.0	−20	23	01	283.22	−47.10	1778

Note: The positions and velocities are from the NASA Extra-galactic Database (NED).

Column 1: Serial number; **Column 2**: Name of the galaxy; **Columns 3 & 4**: Equatorial coordinates in the J2000 epoch; **Columns 5 & 6**: Super Galactic coordinates; **Column 7**: Heliocentric velocity (optical definition).

Table 3. Optical and HI properties of galaxies.

#	Name	Morph.	H.T.	B_0^T (mag)	K^T (mag)	B – K (mag)	HI Flux (Jy km/s)	W_{20} (km/s)
1	NGC 1297	S0a	−2.3	12.65	8.93	3.72		
2	NGC 1309	Sbc	4.0	11.83	9.10	2.73	18.7	171
3	NGC 1315	S0	−1.0	13.38	9.73	3.65		
4	SGC 0321.2-1929	Im	10.0				3.1	79
5	UGCA 068	Scdm	8.7	13.56			5.9	131
6	NGC 1325	Sbc	4.0	11.51	8.63	2.88	24.4	348
7	ESO 548-G 016	S?		14.61				
8	NGC 1332	S0	−3.0	11.21	7.05	4.16		
9	NGC 1331	E/S0	−5.0	14.22	10.76	3.46		
10	APMBGC 548 + 070 + 070	S0			11.23			
11	ESO 548-G 021	Sdm						
12	ESO 548-G 025	Sa	0.7	14.47				
13	NGC 1345	Sc	4.5	13.80			12.0	138
14	NGC 1347	Scd	5.3	13.55			0.6	105
15	NGC 1353	Sbc	3.0	11.73	8.11	3.62		
16	UGCA 077	Sdm	9.0	14.36			5.3	158
17	ESO 482-G 005	Sdm	8.0	14.33			5.4	184
18	IC 1952	Sbc	4.0	12.59	9.87	2.72	5.1	263
19	ESO 548-G 036	S?			10.43		4.1	
20	IC 1953	Sc	7.0	12.10	9.65	2.45	8.1	197
21	NGC 1359	Scm	9.0	12.37	11.17	1.20	25.7	223
22	ESO 548-G 043	Sa		15.55	11.46	4.09		
23	ESO 548-G 044	S0/a	−1.3	14.11	10.37	3.74		
24	NGC 1371	Sa	1.0	11.36	7.63	3.73	53.7	427
25	NGC 1370	E/S0	−3.5	13.36	9.87	3.49		
26	ESO 548-G 049	S?		14.92				
27	IC 1962	Sdm	8.0	13.74			5.5	171
28	NGC 1377	S0	−2.0	13.29	9.72	3.57		
29	ESO 482-G 013	Sb					2.0	99
30	NGC 1385	Scd	6.0	11.14	8.57	2.57	22.6	204
31	NGC 1383	S0	−2.0	13.25	9.44	3.81		
32	NGC 1390	S0/a	1.0	14.01	11.54	2.47	2.4	191
33	NGC 1393	S0	−1.9	12.78	9.18	3.60		

Table 3. *(Continued)*

#	Name	Morph.	H.T.	B_0^T (mag)	K^T (mag)	B – K (mag)	H I Flux (Jy km/s)	W_{20} (km/s)
34	NGC 1401	S0	−2.0	13.11	9.35	3.76		
35	ESO 548-G 064	S0		14.52	10.73	3.79		
36	ESO 548-G 065	Sa	0.7	14.56	12.90	1.66	2.0	145
37	IC 0343	S0	−1.0	13.91	10.50	3.41		
38	NGC 1407	E0	−5.0	10.71	6.70	4.01		
39	ESO 482-G 031	dS0			12.37			
40	APMBGC 548-110-078	dS0						
41	NGC 1415	S0/a	0.0	12.41	8.73	3.68		
42	NGC 1414	Sbc	3.8	13.59			2.1	
43	ESO 548-G 072	S?						
44	NGC 1416	E/S0	−5.0	13.88	10.54	3.34		
45	IC 0345	S0/a		14.64	10.05	4.59		
46	ESO 482-G 035	Sab	2.1	13.42			4.2	177
47	NGC 1422	Sab	2.4	13.16	10.73	2.43		
48	IC 0346	S0	−0.8	13.37	9.78	3.59		
49	ESO 549-G 002	Im	10.0	14.53				
50	MCG-03-10-041	Sdm	8.0		11.91		3.7	184
51	NGC 1440	S0	−1.9	12.35	8.20	4.15		
52	NGC 1438	S0/a	0.0	12.94	9.62	3.32		
53	NGC 1452	Sa	0.4	12.56	8.67	3.89		
54	ESO 549-G 018	Sc	5.0	13.13	10.64	2.49		
55	NGC 1481	S0	−3.3	14.40	11.18	3.22		
56	NGC 1482	S0/a	−0.8	13.01	8.48	4.53	5.5	131
57	ESO 549-G 035	Sc					6.0	145

Note: The morphological types, Hubble types, and photographic B-band magnitudes are from RC3 (third reference catalog of galaxies; de Vaucouleurs *et al.* 1991) provided by NED. The K-band magnitudes are from the *Two Micron All Sky Survey* (2MASS; Jarrett *et al.* 2000). The single dish H I flux integrals and H I widths are from NED.

Column 1: Serial number; **Column 2**: Name of the galaxy; **Column 3**: Morphological type; **Column 4**: Hubble type; **Column 5**: Apparent total photographic B-band magnitude corrected for inclination; **Column 6**: Apparent total K-band magnitude from 2MASS; **Column 7**: B–K color; **Columns 8 & 9**: Single dish H I flux integral (Jy km s^{-1}) and velocity width (km s^{-1}) at 20% of the peak flux density in the global H I profile.

Table 4. Observational details.

#	Date (dd-mm-yy)	Pointing centre α (J2000) (h m s)	δ (J2000) ($^\circ$ $'$ $''$)	Galaxy name	Sepa. (arc min)	rms (mJy/ beam)
1	01-03-00	03 33 47.7	−19 29 31.0	N 1359	0	1.8
2	27-10-00	03 35 01.4	−24 55 58.0	N 1371	0	1.3
3	27-10-00	03 37 28.3	−24 30 05.0	N 1385	0	1.3
4	15-12-00	03 22 06.5	−15 24 00.0	N 1309	0	1.7
5	03-05-01	03 24 25.6	−21 32 39.0	N 1325	0	1.9
6	06-05-01	03 23 25.1	−19 17 04.0	S 0321.2-1929	0	1.3
7	17-05-01	03 54 33.4	−20 28 14.2	N 1482	2.3	1.0
				N 1481	2.8	1.1
				E 549-G 035	8.9	1.4
8	18-05-01	03 40 34.4	−18 30 23.0	A 548-110-078 (×)	4.6	1.0
				N 1407 (×)	6.9	1.1
				I 0343 (×)	7.5	1.1
				A 548-108-069 (×)	8.6	1.1
9	19-05-01	03 27 02.3	−21 16 05.7	N 1332 (×)	4.1	1.1
				E 548-G 016 (×)	5.6	1.1
				N 1331 (×)	5.9	1.1
10	20-05-01	03 45 02.9	−18 15 58.0	N 1440 (×)	0	0.9
11	21-05-01	03 35 14.6	−20 22 25.0	N 1370 (×)	0	0.9
12	22-05-01	03 36 39.1	−20 54 08.0	N 1377 (×)	0	0.9
13	16-06-02	03 29 31.7	−17 46 43.0	N 1345	0	1.5
14	16-06-02	03 32 19.3	−17 43 07.0	U 077	0	1.4
15	17-06-02	03 35 37.3	−21 17 39.1	I 1962	0	0.9
				E 548-G 049	5.1	1.1
16	17-06-02	03 23 47.2	−19 45 15.0	U 068	0	0.9
17	18-06-02	03 41 13.9	−21 41 48.5	N 1414	4.0	0.9
				N 1422	4.1	1.0
18	20-06-02	03 40 56.8	−22 38 24.5	E 482-G 031 (×)	3.6	0.9
				N 1415	4.5	0.9
				N 1416 (×)	4.9	0.9
19	22-06-02	03 29 21.1	−22 12 43.9	E 548-G 025 (×)	6.2	1.2
				N 1347	6.3	1.2
20	23-06-02	03 33 26.5	−23 42 41.0	I 1952	0	1.2
21	23-06-02	03 33 34.5	−21 30 58.7	I 1953	2.8	1.4
				E 548-G 036	3.3	1.4

Table 4. *(Continued)*

#	Date (dd-mm-yy)	Pointing centre α (J2000) (h m s)	δ (J2000) (° ′ ″)	Galaxy name	Sepa. (arc min)	rms (mJy/beam)
22	24-06-02	03 27 35.3	−21 13 42.0	E 548-G 021	0	0.9
23	24-06-02	03 37 52.2	−19 00 30.0	N 1390	0	1.1
24	26-06-02	03 41 15.0	−23 50 10.0	E 482-G 035	0	1.2
25	26-06-02	03 48 14.1	−21 28 28.0	E 549-G 018	0	1.4
26	27-06-02	03 40 31.4	−19 24 40.0	E 548-G 065	7.3	1.1
				E 548-G 072	7.3	1.3
				E 548-G 064 (×)	7.5	1.3
27	27-06-02	03 42 57.3	−19 01 12.0	E 549-G 002	0	1.0
28	28-06-02	03 41 00.3	−19 27 19.0	E 548-G 077 (×)	0	1.2
29	28-06-02	03 43 35.5	−16 00 52.0	M -03-10-041	0	1.2
30	29-06-02	03 33 02.2	−24 07 58.0	E 482-G 005	0	1.1
31	29-06-02	03 36 53.9	−24 54 46.0	E 482-G 013	0	1.1

Notes: **(1)** The bandwidth was 8 MHz except for pointings 5 and 6 where it was 4 MHz and for pointing 4 it was 2 MHz. Therefore, the velocity resolutions were ∼ 13.4 km s^{-1} for all except for N 1325 and S 0321.2-1929 where it was ∼ 6.7 km s^{-1} and for N 1309 it was ∼ 3.3 km s^{-1}.

(2) The on-source integration time for observation was ∼ 3 h except for pointings 5, 6, 7, 8, 9 where it was ∼ 7 h.

(3) The centre frequency was 1412.6 MHz except for pointing 1 (1408.0 MHz), pointings 2 and 3 (1414.0 MHz), pointing 4 (1410.0 MHz), pointings 5 and 6 (∼ 1413 MHz) and pointing 7 (1412.0 MHz).

(4) The column with the heading 'Sepa' indicates the angular separation between the pointing centre and the galaxy.

(5) The $FWHM$ of the image cubes was 20″ × 20″ except for N 1309 and N 1325 where it was 25″ × 25″ and for N 1371, E 482-G 031, N 1415, and N 1416 it was 30′ × 30″.

(6) A cross against the galaxy name indicates an H I non-detection.

Column 1: Serial number; **Column 2**: Date of observation; **Column 3**: Coordinates of the pointing centre; **Column 4**: Galaxies in the field of view; **Column 5**: Separation (arc min) of galaxy(ies) in the field of view from the pointing centre; **Column 6**: RMS noise (mJy $beam^{-1}$) in the channel images.

Table 5. Results from the GMRT H I synthesis observations.

Galaxy name Opt. centre Radio centre ($\alpha(h, m, s)$, $\delta(^\circ\ ,'\ ,''\ )$ J2000)	Type INCL PA	V_{sys} V_{cent} V_{opt} (km/s)	D_{HI} D_{B25} D_{R25} (kpc)	V_{max} V_{flat} $W_{50}/2$ (km/s)	M_{HI} M_K M_{dyn} ($10^9 M_\odot$)	M_{HI}/L_B M_{HI}/L_R M_{HI}/L_K ($M_\odot/L_\odot$)	σ_{HI} (H I) σ_{HI} (opt) D_{HI}/D_{B25} ($M_\odot/pc^2$)
ESO 482-G 005	SBdm	1923	32	80.2	1.08	0.71	1.34
03 33 02.2 -24 07 58	82°	1918	11.3	80.2	–	–	10.7
03 33 2.15 -24 07 58	264°	1915	–	79.5	8.423	–	2.83
ESO 482-G 013	Sb	–	12.9	–	0.578	0.83	4.44
03 36 53.9 -24 54 46	63	1850	7.59	–	0.604	1.5	12.8
03 36 53.8 -24 54 46	65	1835	7.17	–	1.11	0.57	1.7
ESO 482-G 035	SBab	1883	16.4	118	0.438	0.13	2.08
03 41 15.0 -23 50 10	49	1884	12.8	118	4.883	0.2	3.4
03 41 14.7 -23 50 11	185	1890	14.8	115	20.78	0.054	1.28
ESO 548-G 021	SBdm	1690	20	87.7	0.425	0.14	1.36
03 27 35.3 -21 13 42	80	1691	13.4	87.7	0.507	–	3
03 27 35.2 -21 13 41.7	64	1668	–	83.3	11.99	0.5	1.49
ESO 548-G 036	S?	–	–	–	0.257	0.13	–
03 33 27.6 -21 33 53	–	1507	6.7	–	4.482	–	7.31
03 33 28 -21 33 55.1	–	1480	–	60.5	–	0.034	–
ESO 548-G 049	S?	1533	14.9	71	0.296	0.34	1.69
03 35 28.1 -21 13 01	71	1533	6.72	71	–	1.4	8.36
03 35 28.4 -21 13 7.01	128	1510	6.27	–	3.93	–	2.22
ESO 548-G 065	SBa	1213	14.4	72.9	0.289	0.24	1.77
03 40 02.7 -19 22 00	80	1243	10.1	72.9	–	0.78	3.63
03 40 2.53 -19 21 56.8	37	1221	–	64.5	6.214	–	1.43
ESO 548-G 072	S?	2045	8.52	44.3	0.203	0.77	3.56
03 41 00.3 -19 27 19	74	2052	8.74	44.3	–	–	3.38
03 41 0.795 -19 27 19	51	2034	–	48.0	1.989	–	0.975

Table 5. *(Continued)*

Galaxy name Opt. centre Radio centre ($\alpha(h,m,s)$, $\delta(°,','')$ J2000)	Type INCL PA	V_{sys} V_{cent} V_{opt} (km/s)	D_{HI} D_{B25} D_{R25} (kpc)	V_{max} V_{flat} $W_{50}/2$ (km/s)	M_{HI} M_K M_{dyn} ($10^9 M_\odot$)	M_{HI}/L_B M_{HI}/L_R M_{HI}/L_K ($M_\odot/L_\odot$)	σ_{HI} (HI) σ_{HI} (opt) D_{HI}/D_{B25} ($M_\odot/pc^2$)
ESO 549-G 002	IBm	1110	9	55.9	0.189	0.15	2.97
03 42 57.3 -19 01 12	63	1115	8.74	55.9	–	0.32	3.15
03 42 57.2 -19 01 11.1	210	1111	–	60.8	3.167	–	1.03
ESO 549-G 018	SABc	1587	15.5	–	0.429	0.094	2.26
03 48 14.1 -21 28 28	56	1576	17.5	–	12.37	0.13	1.79
03 48 14 -21 28 28.9	203	1587	17.5	152	–	0.021	0.89
ESO 549-G 035	Sc	1814	14.7	74.5	0.526	0.98	3.11
03 55 04.0-20 23 01	56	1768	9.41	74.5	–	–	7.57
03 55 4.39-20 23 0.92	30	1778	–	81.3	6.057	–	1.56
IC 1952	SBbc	1820	19.7	134	0.825	0.11	2.72
03 33 26.7 -23 42 46	71	1823	17.5	134	9.599	0.23	3.44
03 33 26.4 -23 42 46.1	319	1812	22.4	122	36.12	0.052	1.13
IC 1953	SBd	1863	21.3	150	1.46	0.12	4.11
03 33 41.9 -21 28 43	37	1863	18.8	150	20.97	0.2	5.27
03 33 42.2 -21 28 39.3	129	1867	24.2	142	48.78	0.042	1.13
IC 1962	SBdm	1806	26.6	82.3	0.855	0.33	1.54
03 35 37.4 -21 17 33	80	1811	18.1	82.3	0.7401	1.2	3.31
03 35 37.8 -21 17 38	358	1806	18.4	69.1	14.26	0.69	1.47
MCG-03-10-041	SBdm	1207	19.2	110	0.938	–	3.25
03 43 35.5 -16 00 52	57	1217	13.4	110	2.112	0.77	6.61
03 43 35.4 -16 0 51.3	343	1215	13.9	109	18.9	0.27	1.43
NGC 1309	SAbc	2134	24.1	164	3.33	0.22	7.28
03 22 06.5 -15 24 00	20	2134	14.8	164	16.44	0.53	19.4
03 22 5.89 -15 23 59.9	210	2135	13.4	168	46.35	0.12	1.63